Nuclear Science and Techniques (2026) 37:70
https://doi.org/10.1007/s41365-025-01877-z

Nuclear heating at the JSI TRIGA reactor: measurements and simulations

Klemen Ambrožič[1,2] · Hubert Carcreff[3] · Vladimir Radulović[1,2] · Damien Fourmentel[4] · Christophe Destouches[5] · Nicolas Thiollay[5] · Luka Snoj[1,2]

Received: 15 April 2025 / Revised: 12 June 2025 / Accepted: 17 July 2025 / Published online: 2 February 2026

Abstract

Nuclear heating plays an important aspect in design and deployment of both fission and fusion reactors and experimental devices in terms of cooling requirements. Two experimental campaigns in the framework of a collaboration project between the French Atomic and Alternative Energy Commission (CEA) and Jožef Stefan Institute (JSI), Slovenia, have been performed at the JSI TRIGA reactor for the experimental assessment of nuclear heating in fission and fusion-relevant materials by the differential calorimetry technique, based on the CALMOS and CARMEN differential calorimeters, previously developed at CEA. The results of the first campaign performed at reactor powers between 100 and 250 kW have already been reported, highlighting some measurement difficulties. Therefore, the second campaign was performed at a lower reactor power of 30 kW to overcome these issues. Moreover, a computational analysis of the experiments was performed using the JSIR2S code package to calculate the nuclear heating levels. Both experiments and their reproduction by simulations are described in detail. We present a comparison of the previously reported measured nuclear heating values of the first campaign with the computational results, with consistent underestimation by simulations by 8–35%. We report the experimental and computational results for the second experimental campaign performed at a reactor power of 30 kW. The simulated heating values were in agreement with the measurements within the measured heating uncertainty, with simulated heating 2.7–11.3% lower than the experimental values.

Keywords Nuclear heating · Differential calorimeter · R2S · MCNP · Eurofer97 · Tungsten

1 Introduction

When ionizing radiation passes through matter, it transfers its energy to the bulk material, which manifests as material heating. Charged particles interact with matter via both nuclear and electrostatic forces and usually deposit their energies over a short path length. On the other hand, electrically neutral particles such as high-energy photons and neutrons interact via electro-magnetic and nuclear reactions and can generally travel over a significant distance between interactions [1].

Fission and fusion nuclear reactors are intense sources of various types of radiation, from neutrons, high-energy photons to electrons, light and heavy ions. However, owing to the above mentioned reasons, charged particles either lose most of their energy at the location of origin, whereas neutral particles can transfer their energies further away, for instance, to structural or other components. In some cases, components must be kept at cryogenic temperatures,

---

This work was supported by the Slovenian Research Agency (research project NC-0001-Analysis of nuclear heating in a reactor, research core funding Reactor physics No. P2-0073, and infrastructure program I0-0005).

✉ Klemen Ambrožič
klemen.ambrozic@ijs.si

[1] Reactor Physics Division F8, Jožef Stefan Institute, Jamova cesta 39, 1000 Ljubljana, Slovenia

[2] Faculty of Mathematics and Physics, University of Ljubljana, Jadranska cesta 19, 1000 Ljubljana, Slovenia

[3] CEA, Service d'études des réacteurs et de mathématiques appliquées, Université Paris-Saclay, 91191 Gif-sur-Yvette, France

[4] CEA, DES, DEC, IRESNE, DEC, CEA Cadarache, Building 707, 13108 St Paul Lez Durance, France

[5] DES, IRESNE, DER, SPESI, CEA Cadarache, Building 707, 13108 St Paul Lez Durance, France

at which the cooling power requirements scale by a factor 100 to 1000 times the heat removal rate owing to the Carnot efficiency of 1.4% and common helium cooling plant efficiencies of between 20% to 35% [2–5]. The heating rate of such devices can range from a few mWg^{-1} in low power devices [6] to several Wg^{-1} in high power fission [7] and fusion reactors [8] directly due to incident radiation and activation products [9–11], which must be evacuated for stable and safe operation.

When considering neutron and gamma radiation energy deposition, their mechanisms are quite different. Neutrons deposit most of their energy via scattering, which is most effective with light materials. On the other hand, the energy deposition for gamma rays is proportional to some power of the atomic number Z. This implies that gamma radiation is more effective for energy deposition in structural materials commonly used in various nuclear devices than neutrons.

Various particle transport methods are used to quantify the nuclear heating rate and use an effective heating cross section Σ_{heat}, which is derived from basic nuclear data during the processing stage and is subject to user-specified parameters. The validation of computational schemes is performed by faithfully modeling and reproducing high-quality experiments.

In this study, we present the results of two experimental campaigns performed at the JSI TRIGA reactor on nuclear heating measurements in various fission and fusion-relevant materials, and compare them to the calculated heating values using the JSIR2S code [12] by accurate modeling. The heating rates of aluminum, Eurofer97 and tungsten were measured using differential calorimeters based on the CALMOS [13] and CARMEN [14] differential calorimeter designs developed by CEA for the OSIRIS material testing reactor (MTR). The calorimeter design was adapted to lower heating rates and spatial constraints specific to the JSI TRIGA reactor.

In the initial stages of the design, the neutron and gamma heating rate calculations were performed using the MCNP particle transport code [15] in various materials, without considering the self-shielding effect, to assess the expected heating values. Each material sample has unique self-shielding properties and the analysis progressed by including the self-shielding effects by imposing a maximum radiation field attenuation limit of 5%, governing the sample's size. Each calorimeter was equipped with a four-lead constantan wire heating element, wound inside the alumina pearl and embedded in the calorimeter pedestal, close to the material sample, allowing for the simulation of nuclear heating via electric current injection. The heat transfer was modeled using COMSOL Multiphysics [16] to establish the expected increases in the calorimeter cold and hot spot temperature differences and their time constants with the final design changes [17]. A series of calorimeters with different material samples were constructed, with each undergoing a rigorous calibration procedure, where heating was performed using the embedded electrical heater.

Two experimental campaigns were carried out at the JSI TRIGA reactor [18], the initial one in 2021 at reactor power levels of 100 kW and 250 kW, respectively, with findings reported in [6], where deviations from the expected responses were observed, attributed to nonlinear calorimeter calibration responses. In 2022, a second experimental campaign was conducted at a lower reactor power level of 30 kW to minimize nonlinear calibration effects.

Both campaigns were reproduced by detailed simulations using the JSIR2S code [12], which couples a modified version of the MCNP 6.1 code [15] with the FISPACT-II inventory code [19] to determine the delayed gamma contribution.

In this paper, both experimental campaigns are briefly described, followed by a description of the modeling steps. The paper concludes with a comparison of the calculated results with the measurements and a proposal for future improvements and developments.

2 Experiments

Experiments were performed using a custom-designed differential calorimeter at the JSI TRIGA reactor, both of which are described in this section, along with the specifics of individual experimental campaigns.

2.1 Calorimeter

A differential calorimeter sensor for nuclear heating measurements at levels expected in the JSI TRIGA reactor was developed, adapted from the previous CALMOS [13] and CARMEN [14] designs, which were previously used in the OSIRIS reactor. The design is based on a material sample, connected via a thin neck to a heatsink. Thermocouple temperature sensors were placed at each end of the neck. The original designs incorporated cells in a single capsule to form a differential calorimeter: one with a material sample and one serving as a reference. However, the design was updated to a single cell owing to size constraints, with a separate reference sensor with no material sample. Both the reference calorimeter cell and calorimeter cells with the sample material were irradiated at exactly the same position in the central irradiation channel, constrained by the central irradiation channel walls and a bespoke calorimeter cell spacer at the bottom (Sect. 3). During the calorimeter cell replacement, the reactor was shut down and restarted in exactly the same position. Owing to the small sample volume and selection of sample material, no reactivity effects were observed during the calorimeter cell exchange from the reference to the material sample cell.

Nuclear heating was assessed in materials, commonly used in fission and fusion reactors, such as aluminum, graphite, Eurofer97 steel, tungsten and Nb_3Sn superconductors. As with the previous calorimeter sensor types, the samples were in the form of a hollow cylinder; however, the contact between the material sample and the sensor body was on the inner cylindrical surface of the sample, which allowed for a single calorimeter design accommodating different thicknesses of material samples, as shown in Table 1. The initial assessment of the expected nuclear heating values was performed by calculating both neutron and gamma energy depositions without explicitly modeling the sample material. This was done using the calculated incident neutron and gamma flux, spectrum, and neutron and gamma heating cross sections, neglecting the self-shielding and self-attenuation effects (gamma field depression in the sample thickness) [20]. As expected, the gamma component of the total heating was an order of magnitude greater than the neutron component. Additional calculations were performed to quantify the self-attenuation in the material samples, i.e., to determine the maximal sample outer diameter, which does not significantly perturb or attenuate the incident radiation field and change its underlying heating effect. The attenuation limit was set at 5%, as a compromise between incident field perturbation and energy deposition. In addition to the aforementioned constraints in terms of size, expected heating rate and perturbation, one of the requirements was to include an electrical heating element for calorimeter calibration. The heating element consisted of a constantan wire wound inside an alumina pearl, which acted as an electric insulator and supported the wire. The wire has four electrical connections for the precise measurement of the injected power via separate voltage and current intensity, independently of the wire resistance variation. In addition to the calibration process, an electrical heater is also necessary for the inference of nuclear heating using the zero method, which is mentioned below. The structural material of the sensor was stainless steel, which has lower thermal conductivity than aluminum. This, combined with the high sensor sensitivity due to the reduced diameter of the pedestal, resulted in a significant temperature stabilization time of approximately 40 min. After establishing the expected heating values, sample material sizes and other requirements, a calorimeter sensor design was modeled, and the expected temperature profiles and stabilization times were calculated using the COMSOL Multiphysics package [16] to obtain the final sensor design. The results of these analyses are reported in Ref. [17], and the final calorimeter sensor design is shown in Figs. 1 and 2. The manufacturing of the Nb_3Sn superconductor sample was unfortunately not successful because of the unfavorable mechanical properties of the Nb_3Sn material; hence, heating rate measurements with this material were not performed.

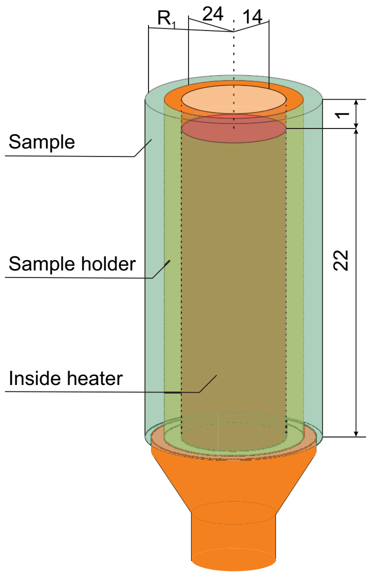

Fig. 1 (Color online) Schematic view of the calorimeter head with heater and the material sample

Table 1 Radii R_1 and the corresponding sample thicknesses for different materials

Sample material	Sample thickness (mm)	Radius R_1 (mm)
Aluminum	2.0	4.4
Eurofer97	1.1	3.5
Tungsten	0.1	2.5

Upon manufacturing, the calorimeters were calibrated in a test water tank facility, as shown in Fig. 3, where temperature differences corresponding to injected electrical power were determined, representing the basis for the measurements in the JSI TRIGA reactor by covering the entire expected heating range at different reactor power levels. This procedure yielded two sets of calibration coefficients relating the temperature difference between the hot and cold temperature measurement points: linear, i.e., first-order dependence of the temperature difference to the injected electrical power, valid up to 0.1 W of injected power, and nonlinear, 3rd-order polynomial coefficients, covering the range of 0W to 0.5W. Such higher-order dependence is commonly used in calorimetry techniques [21–25]. In this particular case, it stems from the fact that the specific heat capacity depends on the temperature, radiative losses and changes in thermal contact because the sample material is press-fit to the sample holder. Hence, a 3rd-order polynomial fit was used.

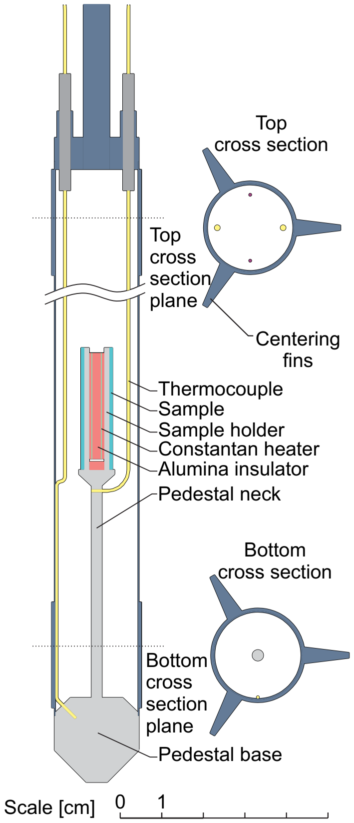

Fig. 2 Detailed drawing of the calorimeter sensor used during the experiments. Hot and cold thermocouples are used to measure the temperature difference

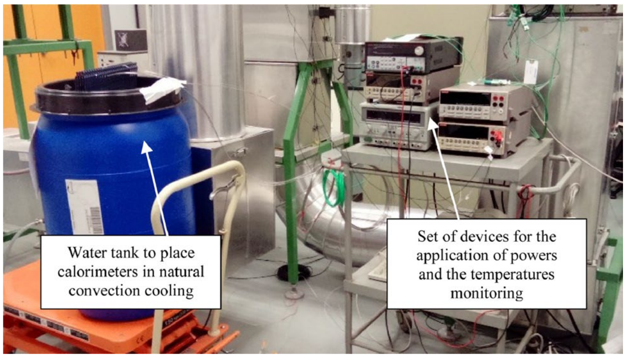

Fig. 3 (Color online) Calibration water tank with associated measurement and heating equipment

Two different techniques were used to measure nuclear heating.

- $\Delta\Delta T$ technique: The temperature difference ΔT_{mat} between the hot and cold thermocouple is measured in order to determine the heating contribution of the entire sensor equipped with the material sample. Another temperature difference measurement ΔT_{ref} was performed in the same radiation field using a calorimeter without the sample material (the reference) to determine the heating rate of the calorimeter structure only. The difference $\Delta\Delta T = \Delta T_{\mathrm{mat}} - \Delta T_{\mathrm{ref}}$ is then used to determine the nuclear heating in the actual sample on the basis of the calibration data.
- Zero method: The temperature difference ΔT_{mat} is measured in the calorimeter with the sample material. The reference calorimeter without the sample material is positioned inside the same radiation field, and electrical power is applied to the heater, until $\Delta T_{\mathrm{mat}} = \Delta T_{\mathrm{ref}}$ is satisfied, at which point the injected electrical power corresponds to nuclear heating in the sample.

It can be observed that the underlying assumption is that both the calorimeter with the sample material and the reference calorimeter are exposed to the same radiation field. This means that the measurement should be performed in the same position and under the same experimental conditions, that is, the same core configuration, control rod position and duration of the power excursion. The measurements were conducted in an aluminum irradiation channel located at the central (A1) position of the JSI TRIGA reactor core. The channel had custom holes that allowed the ingress of cooling water into the channel, serving as a calorimeter heatsink. An aluminum spacer with a length of 221 mm was manufactured and inserted in the irradiation channel to achieve consistent centering of the sample material at the core mid plane. For consistent positioning in the horizontal plane, the calorimeter sensors were equipped with fins, which centered the sensor inside the irradiation channel and served as an effective heat spreader, maintaining the calorimeter pedestal base at the temperature of the surrounding cooling water.

2.2 JSI TRIGA reactor

The JSI TRIGA reactor is a pool-type reactor with a maximum steady state thermal power of 250 kW. The reactor core is submerged approximately 490 cm below the water surface, as shown in Figs. 4 and 5. It consists of 91 positions in an annular configuration arranged in 6 concentric rings. 4 positions are taken by the control rods, and the rest can be either empty, filled with fuel elements or irradiation positions, which can be dry or filled with water [18]. Two irradiation positions—triangular channels—occupy three fuel element positions. The in-core irradiation channels are shown schematically in Fig. 6. The core is surrounded by a graphite reflector, which houses a rotary carousel irradiation facility with 40 positions. Aside from the in-core irradiation positions, there are several larger horizontal ports: tangential, radial beam and radial piercing ports, and 2 two larger ex-core irradiation facilities: the thermalizing and thermal columns.

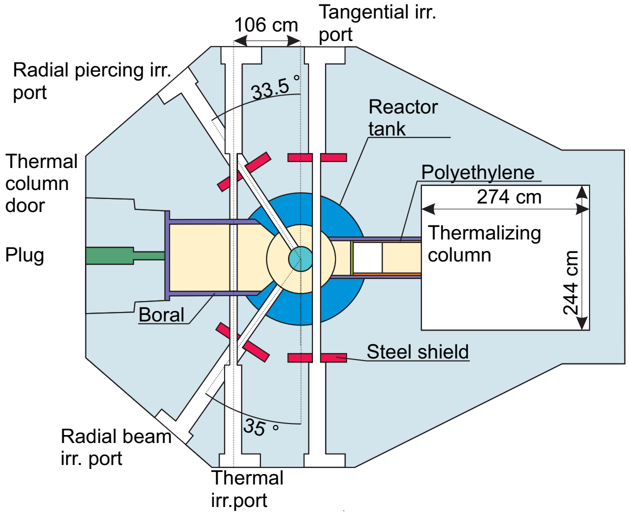

Fig. 4 (Color online) Top view of the JSI TRIGA reactor with thermal and thermalizing column, and the horizontal irradiation ports

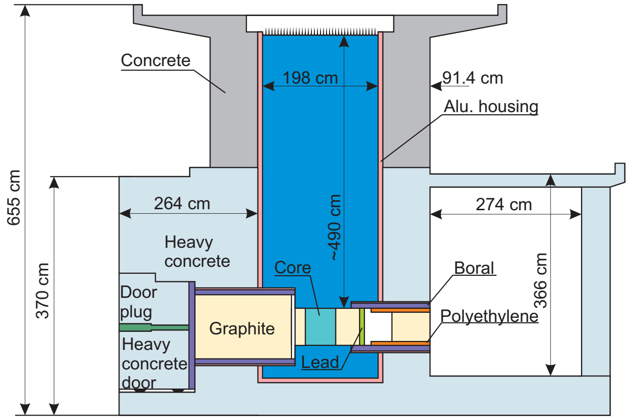

Fig. 5 (Color online) Side view of the JSI TRIGA reactor, showing the core inside the reactor tank, as well as larger thermal and thermalizing column facilities

The fuel elements are schematically displayed in Fig. 6, consist of a central Zr rod, a homogeneous mixture of fuel and moderator in the U-ZrH form, with graphite reflectors on top and bottom and clad in stainless steel. The reactor core and internal structures around the core are shown schematically in Fig. 7. Two similar reactor core loading patterns were used for the two experiments, as shown in Fig. 8. In both cases, the calorimeter was inserted into the A1—central position inside a wet thin-wall irradiation channel (Fig. 6), which has holes on the side, allowing for the exchange of water. Both triangular channels were inserted during the experiments.

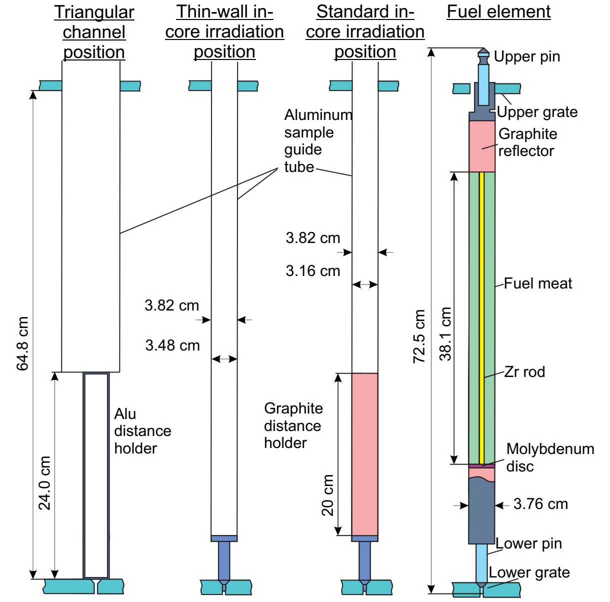

Fig. 6 (Color online) TRIGA in-core irradiation channels and fuel element

2.3 Experimental campaigns

Design basis calculations and calibration procedures were performed for full reactor power operation. This is why the first experimental campaign was performed in July 2021 at reactor power of 100 kW to 250 kW, respectively. During the preliminary measurements of the campaign, the readings from the calorimeter sensor equipped with the graphite sample were erratic and unreliable and were not further evaluated.

The reactor power level and control rod positions for 1st and 2nd experimental campaigns are reported in Tables 2 and 3, respectively. The detailed time-dependent control rod positions and reactor power plots for each calorimeter irradiation are displayed in Fig. S1 and Fig. S2 of the Supplementary Material for the 1st and 2nd experimental campaigns, respectively. The measured temperature time series for the 1st campaign are also provided. The methodology for obtaining the nuclear heating results differed slightly between the two experimental campaigns. The calibration data showed a linear dependence of the temperature difference for low applied heating power up to approximately 0.1 W and a nonlinear regime for higher applied heating power. During the 1st campaign, the measured heating rates were in the nonlinear regime; therefore, the heating rate results were inferred from higher-order calibration curves fitted to the calibration data, as well as the current injection, i.e., the zero method. The results obtained using the linear calibration curve differed significantly from those obtained using the other two methods and were therefore not considered,

Fig. 7 (Color online) Reactor core and internal structures around the core

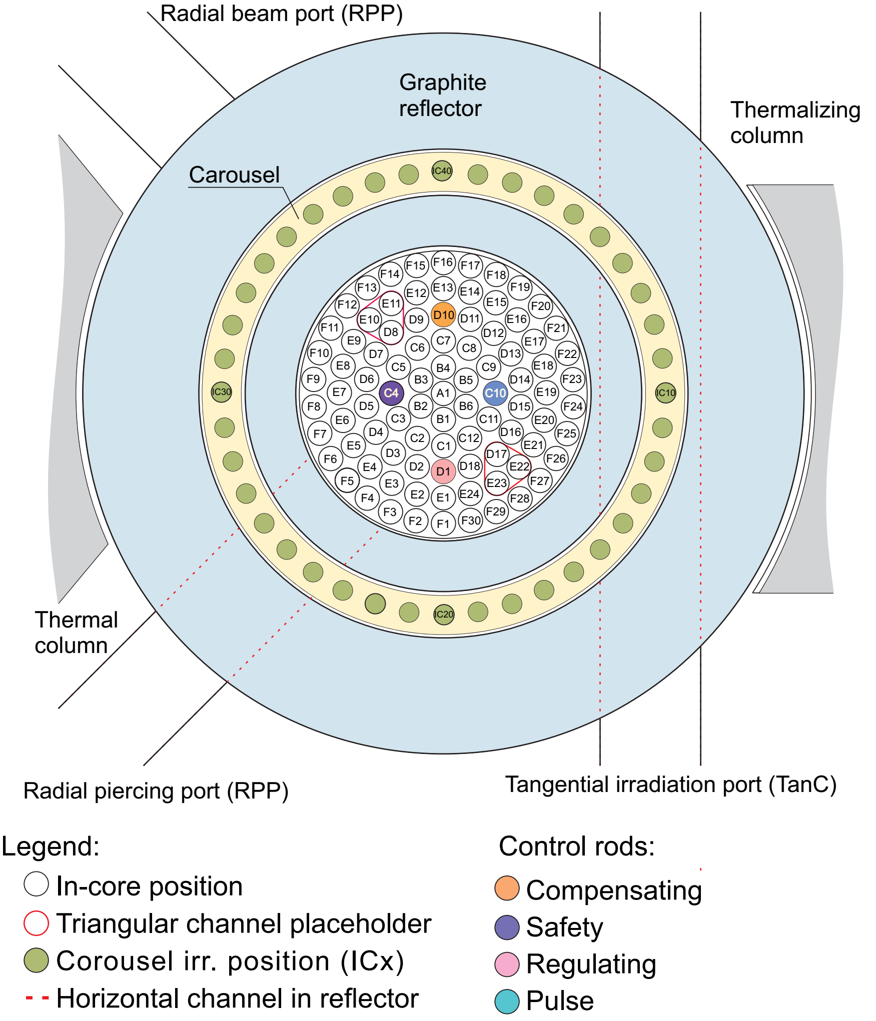

as discussed in Ref. [6]. This was addressed during the 2nd campaign, where irradiations were performed at a lower reactor power of 30 kW to remain in the linear regime with lower heating rates. The heating values obtained during the 1st campaign are displayed in Table 4, while the results obtained during the 2nd campaign are presented in Table 5. The measured nuclear heating uncertainties were calculated based on the evaluated uncertainty of the reactor power [26] and as a 1σ standard deviation of nuclear heating evaluations using both the Zero and $\Delta\Delta T$ methods in combination with linear and higher-order calibration curves.

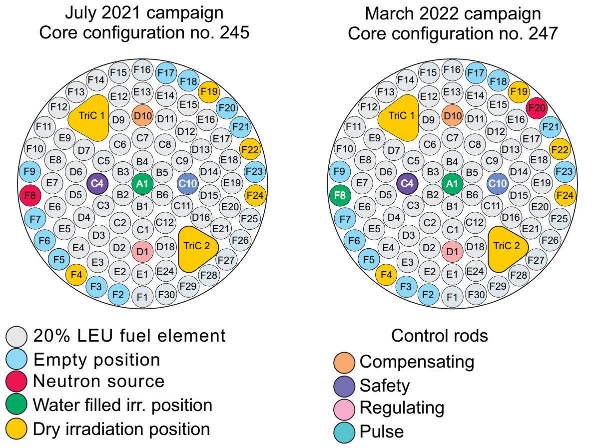

Fig. 8 (Color online) Reactor core configuration during the 1st (left) and 2nd (right) experimental campaign

3 Computational modeling

Nuclear heating was modeled using the Monte Carlo particle transport code MCNP [15], for the transport of both prompt and delayed particles, including neutron and photon transport. Electron transport was modeled only inside the sample material, calorimeter body and irradiation channel, to reduce the computational time but still calculate the energy deposition rate without the kerma approximation.

Table 2 Reactor power and control rod configurations for nuclear heating experiments during the 1st experimental campaign

Sample material	Reactor power (kW)	Control rod							
		Safety		Regulating		Compensating		Transient	
		% out	pos.	% out	pos.	% out	pos.	% out	pos.
Aluminum	100	100	200	57.7	484	57.1	500	100	0
Aluminum	250	100	200	65.9	470	66.5	434	100	0
Eurofer97	100	100	200	54.8	506	57.1	500	100	0
Eurofer97	250	100	200	63.0	447	65.7	441	100	0
Tungsten	100	100	200	57.0	490	57.1	500	100	0
Tungsten	250	100	200	64.4	437	66.3	436	100	0

% out and pos. denote the percentage of control rod withdrawn and the rod position as given by the reactor instrumentation, respectively

Table 3 Reactor control rod configurations for nuclear heating experiments during the 2nd experimental campaign at reactor power of 30 kW

Sample material	Control rod							
	Safety		Regulating		Compensating		Transient	
	% out	pos.	% out	pos.	% out	pos.	% out	pos.
Aluminum	100	200	55.2	503	57.1	500	100	0
Eurofer97	100	200	53.1	518	54.6	518	100	0
Tungsten	100	200	52.7	521	54.6	518	100	0

Table 4 Nuclear heating measurements and their 1σ uncertainties of the 1st campaign at different reactor power levels

Material	Reactor power (kW)	Heating (mW/g)	Heating per reactor power (mW/g kW)
Aluminum	100	53.8 ± 8.4	0.538 ± 0.084
Aluminum	250	131.0 ± 20.0	0.524 ± 0.080
Eurofer97	100	52.8 ± 1.1	0.528 ± 0.011
Eurofer97	250	129.0 ± 2.8	0.516 ± 0.112
Tungsten	100	112.6 ± 3.2	1.126 ± 0.032
Tungsten	250	275.0 ± 8.4	1.100 ± 0.034

Table 5 Nuclear heating measurement and their 1σ uncertainties of the 2nd campaign at reactor power of 30 kW

Material	Heating (mW/g)	Heating per reactor power (mW/g kW)
Aluminum	13.1 ± 3.3	0.437 ± 0.11
Eurofer97	15.1 ± 0.6	0.503 ± 0.02
Tungsten	35.2 ± 4.0	1.173 ± 0.13

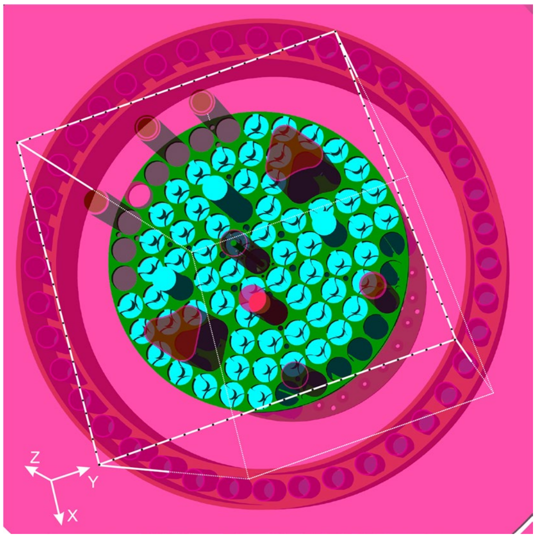

Fig. 9 (Color online) Mesh outer boundaries superimposed over MCNP model of reactor core and the calorimeter with Eurofer97 sample from the 2nd experimental campaign. 25×25 voxels in X–Y direction, and 50 voxels in Z direction

The ENDF/B-VIII.0 [27] nuclear data libraries [27] were used throughout the modeling.

A detailed MCNP model of the JSI TRIGA reactor was used based on the criticality benchmark model [28]. The model was expanded by introducing irradiation channels and verified control rod positions [29] as well as new triangular irradiation channels [30]. Fresh fuel was used. The reactor model core configuration and control rod positions were modified to reflect the configurations used during the experiments. A 3D ray-traced image of the JSI TRIGA MCNP model used in the 2nd campaign is displayed in Fig. 9.

The calorimeters, including the material samples within, as well as the supporting structures, such as the bottom spacer, connecting cables and coupler for calorimeter insertion and withdrawal, were modeled in great detail. A 3D ray-traced image of the calorimeter and supporting structures inserted inside the wet thin-wall irradiation channel is displayed in Figs. 10 and 11.

Two separate simulation steps were performed to model the heating from both prompt and the delayed gamma rays, the latter owing to the decay of fission and activation products. In the first step, calculations were performed in the criticality mode, and the heating due to prompt radiation was calculated inside the sample over a cylindrical mesh corresponding to the sample dimensions. The energy deposition was calculated separately for neutrons, gamma rays in the kerma approximation, and electrons, as well as the total energy deposition using the TMESH functionality of the MCNP code. The effective multiplication factor k_{eff} and number of neutrons per fission $\bar{\nu}$ were also obtained for each individual simulation for power normalization using the formulation described in [31]. The reactor power, as measured by the reactor instrumentation [26], was used to normalize the heating level inside the sample at the readout time.

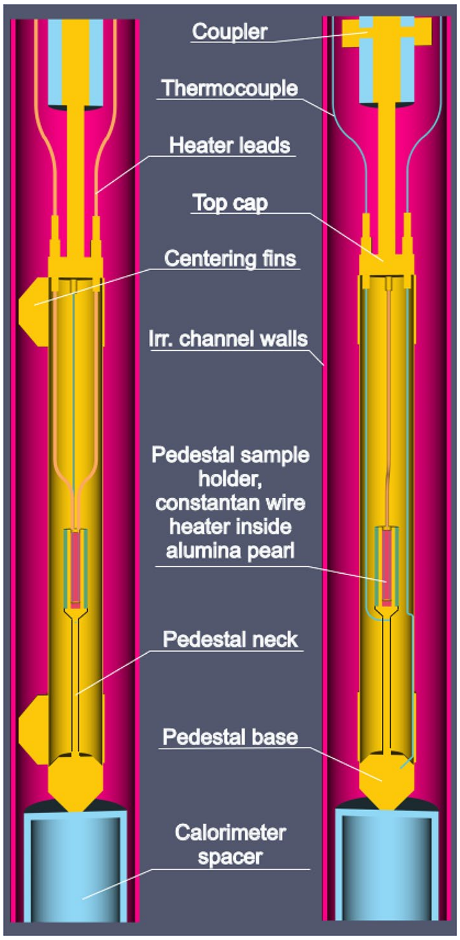

Fig. 10 (Color online) Ray-traced calorimeter MCNP model, side-views

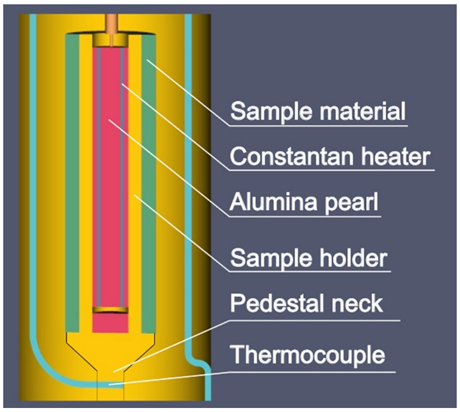

Fig. 11 (Color online) Close-up of the ray-traced calorimeter model: the pedestal and accompanying components

For the simulation and transport of the delayed radiation owing to the decay of fission and activation products, the JSIR2S code was used. The code utilizes the cell-under-voxel approach, where a mesh is superimposed over the model geometry, and each part of the geometry is divided into individual mesh pieces. A $2\,\mathrm{cm} \times 2\,\mathrm{cm} \times 2\,\mathrm{cm}$ mesh was superimposed, spanning the entire reactor core, control rods and partially encompassing the graphite reflector as shown in Fig. 9. To calculate the volume-averaged fluxes in each cell-under-voxel, volume calculations in the resulting irregular shapes must be performed using the Monte Carlo method, with the target 1σ accuracy set to $1 \times 10^{-5}\,\mathrm{cm}^3$, primarily because of the small size of the calorimeter and its components.

Once the volumes were calculated, another neutron transport simulation was performed in the criticality mode, and the neutron flux was tallied in each of the above mentioned cells-under-voxel in the CCFE-709 energy group structure [32], which was used for subsequent depletion calculations on a per cell-under-voxel basis. The time-dependent total fluxes were modeled in steps closely following the reactor power readout during the experiments: A change in power step was modeled if the reactor power recorded by the instrumentation differed from the last change by more than 0.5%, resulting in several hundred steps, as displayed in Fig. 12. Changes in k_{eff} and $\bar{\nu}$ due to different control rod positions and the effects of the sample were also considered for the normalization of neutron fluxes. This data, along with the material composition of each cell, were used for the depletion calculations using the FISPACT-II code and ENDF/B-VIII.0 nuclear data libraries. Nuclide vectors were calculated at the time of heating measurements during the experiment and were used to construct a custom secondary particle source description, which was used for delayed particle transport calculations and determination of nuclear heating using the same approach as for prompt heating calculations.

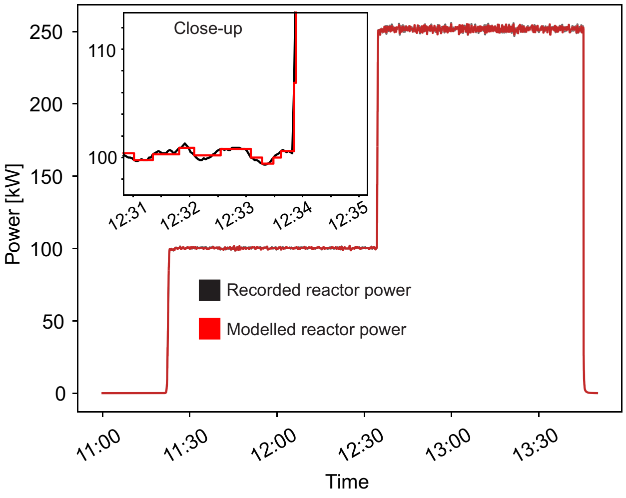

Fig. 12 Recorded and modeled reactor power during the 1st campaign's Eurofer97 sample irradiation

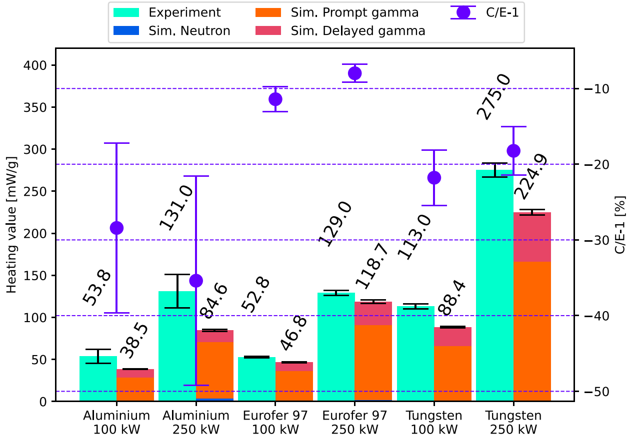

Fig. 13 (Color online) Comparison of measured and calculated nuclear heating values for the 1st campaign, performed at reactor power of 100 kW and 250 kW. Values on top of the individual bars represent the total nuclear heating, with black error bars denoting the 1σ uncertainty. Purple dots and error bars denote the $C/E-1$ values and their uncertainties

Because the material calorimeter samples were of relatively small size, a comparison of the energy deposition due to incident gamma rays was made under the assumption of charged particle equilibrium (in the kerma approximation) and by the transport and energy deposition of secondary charged particles.

The nuclear heating results owing to delayed radiation were then combined with the results for prompt radiation, scaled to the reactor instrumentation power readout at the measurement times, to obtain the total heating rates. The 1σ statistical uncertainty of the Monte Carlo particle transport tallies was considered for the uncertainty estimate. Further effects, such as the accuracy of reactor power modeling, geometrical model inaccuracies, uncertainties in material definitions and nuclear data, were not considered in this study.

4 Comparison of modeled and measured nuclear heating

In this section, we compare the prompt and delayed heating values obtained from computational modeling with the experimental values.

The heating values obtained by the computations were further divided into individual contributions: prompt neutrons and prompt gamma, as well as the contribution of gamma rays due to the decay of fission and activation products. The nuclear heating values obtained experimentally and by computational modeling and their comparison are graphically presented in Figs. 13 and 14 for the 1st and the 2nd campaign, respectively, with numerical values given in Tables S1 and S3 of the Supplementary Materials. The fractions of individual contributions are also reported in Table S2 and S4, respectively. The differences in the modeling frameworks between kerma and dose approximation are presented in Tables S5 and S6, respectively.

The difference between the simulated and measured nuclear heating is significantly higher for the 1st experimental campaign, where nonlinear calorimeter calibration factors were used to estimate the measured nuclear heating values. The $C/E-1$ values range between – 35% to – 28% for aluminum with uncertainty 6%, between – 11% to – 8% for Eurofer97 with 0.4% uncertainty and between – 22% to – 18% with 1% uncertainty for tungsten. The discrepancies appear to be much smaller for the second

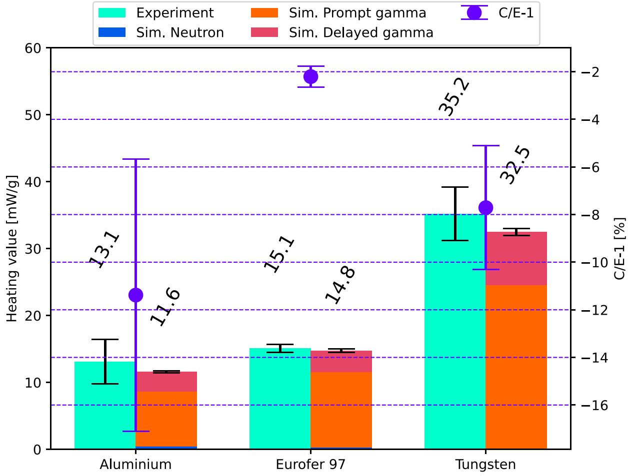

Fig. 14 (Color online) Comparison of measured and calculated nuclear heating values for the 2nd campaign, performed at reactor power of 30 kW. Values on top of the individual bars represent the total nuclear heating, with black error bars denoting the 1σ uncertainty. Purple dots and error bars denote the $C/E-1$ values and their uncertainties

campaign, where special care was taken to irradiate the calorimeter at a sufficiently low power of 30 kW so that the calorimeter response remained in the linear regime. The $C/E-1$ values here are greatly reduced, being -11.5% with a 3% uncertainty for aluminum, 2.5% with a 0.15% uncertainty for Eurofer 97 and -7.8% with a 1% uncertainty for tungsten.

It is interesting to note that the discrepancy between simulations and measured heating values appears to be systematic, and could be attributed to several reasons:

- ENDF/B-VIII.0 nuclear data libraries used in our simulations only include data only for 557 of more than 3000 in total. Moreover, not all of the nuclear data, i.e., reaction cross sections and decay constants have uncertainty data associated with them.
- Model inaccuracies in terms of geometry, material composition and the accuracy of replicating the reactor power in time.

The computational analysis of the above mentioned uncertainties can be performed by random sampling of both nuclear data within their uncertainties [33], as well as sampling the material composition and model geometry within their uncertainties, known as the total Monte Carlo method. However, such an analysis would be very computationally expensive and beyond the scope of this study.

It can also be noted that although the comparison between the measurements and simulations appears to be within their 1σ uncertainties for the most part, the calculated nuclear heating values are systematically below the measurements, which was not the case in previous analyses of nuclear heating and gamma dose rates in the JSI TRIGA reactor [12, 34].

5 Conclusion

We present nuclear heating experiments performed using custom built calorimeter devices, where nuclear heating was measured in aluminum, Eurofer97 and tungsten samples. Two experimental campaigns were performed: the initial one at reactor powers of 100 kW and 250 kW, where the calorimeter responses were determined to be out of the scope of linearity. The second experimental campaign was performed at a much lower reactor power of 30 kW, where the calorimeter response was evaluated to be linear.

Both experimental campaigns were reproduced in great detail, both in terms of model geometry and time-dependent power following. The prompt neutron and gamma radiation were modeled using the MCNP particle transport code, whereas the delayed radiation term was modeled using the JSIR2S code, which coupled the FISPACT-II radioactive inventory calculation code with MCNP.

The agreement between calculated and measured heating values is given, where discrepancies between simulations and measurements for the 1st campaign range between – 12% to – 8% for Eurofer97 and – 21% to – 18% for tungsten, while differences of – 35% to – 28% are observed for aluminum. It is interesting to note that the $C/E-1$ discrepancy did not increase with an increase in reactor power for Eurofer97 and tungsten, which is the case for aluminum, where the effect of the nonlinear response was the most significant.

For the 2nd campaign, performed at a reduced reactor power, the discrepancies were much lower, below 12% for aluminum and within 3% for Eurofer97 and tungsten. The calculated heating is in good agreement with the measured heating values within the uncertainty range of the measured values.

Further analysis using the total Monte Carlo method was proposed to identify the source of the systematic discrepancies between the measured and simulated heating values and to identify sensitivity profiles for perturbations of individual simulation parameters.

Supplementary Information The online version contains supplementary material available at https://doi.org/10.1007/s41365-025-01877-z.

Author Contributions Luka Snoj, Christophe Destouches and Nicolas Thiollay were responsible for project's funding acquisition, administration and supervision. Klemen Ambrožič, Hubert Carcreff, Vladimir Radulović, Damien Fourmentel and Luka Snoj performed the pre-analysis to assess the estimated nuclear heating and determined the calorimeter design. Hubert Carcreff, Damien Fourmentel, Christophe Destouches and Nicolas Thiollay managed the final design, manufacturing and testing of the calorimeter device. Hubert Carcreff, Vladimir Radulović, Damien Fourmentel and Nicolas Thiollay performed the measurements in the JSI TRIGA reactor. Klemen Ambrožič performed the simulation conceptualization and the analysis and the first draft of the manuscript, and all authors commented on previous versions. All authors approved the final manuscript.

Declarations

Conflict of interest The authors declare that they have no Conflict of interest.

References

1. F.H. Attix, *Introduction to Radiological Physics and Radiation Dosimetry* (A Wiley-Interscience publication, Wiley, New York, 1986)

2. P. Dauguet, G.M. Gistau-Baguer, P. Briend et al., Air liquides contribution to the cern lhc refrigeration system. AIP Conf. Proc. **985**, 557–563 (2008). arXiv:https://pubs.aip.org/aip/acp/article-pdf/985/1/557/1168.0534/557_1_online.pdf, https://doi.org/10.1063/1.2908597
3. A. Dalesandro, A. Weiner, J.P. Kelley et al., The SPARC cryogenic system. IOP Conf. Ser. Mater. Sci. Eng. **1301**, 012107 (2024). https://doi.org/10.1088/1757-899X/1301/1/012107
4. P. Lebrun, Cryogenics for the large hadron collider. IEEE Trans. Appl. Supercond. **10**, 1500–1506 (2000). https://doi.org/10.1109/77.828526
5. H. Christine, V. Lamaison, M. Wanner et al., EU DEMO Cryogenic System and Cryodistribution Pre-conceptual design for an optimal cooling of the superconducting magnets and the thermal shields. In *Fusion Energy Conference (FEC 2020),* IAEA, NICE, France, May 2021
6. H. Carcreff, V. Radulovi, D. Fourmentel et al., Nuclear heating measurements for fusion and fission relevant materials in the JSI TRIGA reactor. Fusion Eng. Des. **179**, 113136 (2022). https://doi.org/10.1016/j.fusengdes.2022.113136
7. E. Privas, L. Chabert, Reflector features and physics consideration issued from the Jules Horowitz Reactor design analyses. EPJ Nucl. Sci. Technol. **4**, 18 (2018). https://doi.org/10.1051/epjn/2018040
8. D. Flammini, A. Chaudhary, A. Colangeli et al., Neutronic analyses for the equatorial diagnostic port plug 12 in ITER. Fusion Eng. Des. **193**, 113639 (2023). https://doi.org/10.1016/j.fusengdes.2023.113639
9. A. Žohar, I. Lengar, L. Snoj, Analysis of water activation in fusion and fission nuclear facilities. Fusion Eng. Des. **160**, 111828 (2020). https://doi.org/10.1016/j.fusengdes.2020.111828
10. A. Žohar, A. Pungerčič, K. Ambrožič et al., Analysis of irradiation experiments with activated water radiation source at the JSI TRIGA Research Reactor. Fusion Eng. Des. **161**, 111946 (2020). https://doi.org/10.1016/j.fusengdes.2020.111946
11. D. Kotnik, J. Peric, D. Govekar et al., KATANA-water activation facility at JSI TRIGA, part II: first experiments. Nucl. Eng. Technol. **57**, 103290 (2025). https://doi.org/10.1016/j.net.2024.10.052
12. K. Ambrožič, L. Snoj, JSIR2S code for delayed radiation simulations: validation against measurements at the JSI TRIGA reactor. Prog. Nucl. Energy **129**, 103498 (2020). https://doi.org/10.1016/j.pnucene.2020.103498
13. H. Carcreff, L. Salmon, V. Lepeltier et al., Last improvements of the CALMOS calorimeter dedicated to thermal neutron flux and nuclear heating measurements inside the OSIRIS reactor. EPJ Web Conf. **170**, 04002 (2018). https://doi.org/10.1051/epjconf/201817004002
14. D. Fourmentel, J.F. Villard, A. Lyoussi, et al., Combined analysis of neutron and photon flux measurements for the Jules Horowitz Reactor core mapping. In *2011 2nd International Conference on Advancements in Nuclear Instrumentation, Measurement Methods and their Applications*, Ghent, Belgium, 2011, pp. 1–5. https://doi.org/10.1109/ANIMMA.2011.6172905
15. T. Goorley, M. James, T. Booth et al., Initial MCNP6 release overview. Nucl. Technol. **180**, 298–315 (2012). https://doi.org/10.13182/NT11-135
16. C. AB, Comsol multiphysics®. (2022) www.comsol.com
17. K. Ambrožič, D. Fourmentel, H. Carcreff et al., Computational support on the development of nuclear heating calorimeter detector design. EPJ Web Conf. **225**, 04033 (2020). https://doi.org/10.1051/epjconf/202022504033
18. L. Snoj, K. Ambrožič, L. Barbot et al., A half-century of nuclear research, education and training: story of the JSI TRIGA reactor. Ann. Nucl. Energy **214**, 111122 (2025). https://doi.org/10.1016/j.anucene.2024.111122
19. J.C. Sublet, J. Eastwood, J. Morgan et al., FISPACT-II: an advanced simulation system for activation, transmutation and material modelling. Nucl. Data Sheets **139**, 77–137 (2017). https://doi.org/10.1016/j.nds.2017.01.002
20. S. Accelerators, A. Trkov, G. žerovnik, L. Snoj et al., On the self-shielding factors in neutron activation analysis. Nucl. Instrum. Methods Phys. Res. Sect. A Detectors Assoc. Equipm. **610**, 553–565 (2009). https://doi.org/10.1016/j.nima.2009.08.079
21. A. Volte, M. Carette, A. Lyoussi et al., Study review of the calorre differential calorimeter: definition of designs for different nuclear environments. EPJ Web Conf. **253**, 04016 (2021). https://doi.org/10.1051/epjconf/202125304016
22. J. Rebaud, A. Volte, M. Carette et al., Experimental and numerical results for a new single-cell calorimeter dedicated to nuclear heating rate measurement. EPJ Web Conf. **288**, 04008 (2023). https://doi.org/10.1051/epjconf/202328804008
23. J.G. Berberian, Note: Low temperature calibration of a commercial differential scanning calorimeter. Rev. Sci. Instrum. **89**, 016105 (2018). arXiv:https://pubs.aip.org/aip/rsi/article-pdf/doi/10.1063/1.5005817/16092930/016105_1_online.pdf, https://doi.org/10.1063/1.5005817
24. J. Zhang, T. Ma, L. Zhang et al., The design and calibration of a new differential calorimetric dedicated to nuclear heating measurements. Ann. Nucl. Energy **219**, 111485 (2025). https://doi.org/10.1016/j.anucene.2025.111485
25. V.A. Drebushchak, Calibration coefficient of a heat-flow DSC. Part I. Relation to the Sensitivity of a thermocouple. J. Therm. Anal. Calorim. **76**, 941–947 (2004). https://doi.org/10.1023/B:JTAN.0000032279.21790.f6
26. Ž. Štancar, L. Snoj, An improved thermal power calibration method at the TRIGA Mark II research reactor. Nucl. Eng. Des. **325**, 78–89 (2017). https://doi.org/10.1016/j.nucengdes.2017.10.007
27. D. Brown, M. Chadwick, R. Capote et al., ENDF/B-VIII.0: the 8th major release of the nuclear reaction data library with CIELO-project cross sections, new standards and thermal scattering data. Nucl. Data Sheets **148**, 1–142 (2018). https://doi.org/10.1016/j.nds.2018.02.001
28. R. Jeraj, M. Ravnik, TRIGA Mark II Reactor: U(20)-Zirconium Hydride Fuel Rods in Water with Graphite Reactor, IEU-COMP-THERM-003. In *International Handbook of Evaluated Criticality Safety Benchmark Experiments*, NEA/NSC/DOC(95)03, OECD NEA, Paris France, September 1999
29. L. Snoj, A. Trkov, R. Jaćimović et al., Analysis of neutron flux distribution for the validation of computational methods for the optimization of research reactor utilization. Appl. Radiat. Isot. **69**, 136–141 (2011). https://doi.org/10.1016/j.apradiso.2010.08.019
30. T. Goričanec, S. Rupnik, A. Jazbec et al., On the optimisation of large sample in-core irradiation channel in the JSI TRIGA reactor. In *NENE 2020 Conference Proceedings,* Nuclear Society of Slovenia, 2020
31. G. Žerovnik, M. Podvratnik, L. Snoj, On normalization of fluxes and reaction rates in MCNP criticality calculations. Ann. Nucl. Energy **63**, 126–128 (2014). https://doi.org/10.1016/j.anucene.2013.07.045
32. A.P.J. Hodgson, R.W. Grimes, M.J.D. Rushton et al., The impact of neutron cross section group structures on the accuracy of radiological source models. Nucl. Sci. Eng. **181**, 302–309 (2015). https://doi.org/10.13182/NSE14-156
33. L. Fiorito, G. Žerovnik, A. Stankovskiy et al., Nuclear data uncertainty propagation to integral responses using SANDY. Ann. Nucl. Energy **101**, 359–366 (2017). https://doi.org/10.1016/j.anucene.2016.11.026
34. A. Gruel, K. Ambrožič, C. Destouches et al., Gamma-heating and gamma flux measurements in the JSI TRIGA reactor: results and prospects. IEEE Trans. Nucl. Sci. **67**, 559–567 (2020). https://doi.org/10.1109/TNS.2020.2974968